Research Article

On-Line Monitoring Shaft Misalignment of Feed Drive Systems Based on Time-Domain Shaft Rotating Holospectrum

Y. S. Chiu, C. C. Cheng (ID), W. C. Hsu, and M. H. Huang

Advanced Institute of Manufacturing with High-tech Innovations and Department of Mechanical Engineering,
National Chung Cheng University, No 168, Sec. 1, University Rd., 621 Min-Hsiung Township, Chia-Yi County, Taiwan

Correspondence should be addressed to C. C. Cheng; imeccc@ccu.edu.tw

Detection of early-stage misalignment of the ball screw in feed drive systems is the topic addressed in this study. The triaxial vibration amplitudes and phases of a rotating ball screw at the ball screw nut were extracted using the Vold–Kalman filtering order tracking (VKFOT). The rotating ball screw locus at the rotation speed and its multiplier in the time domain were then constructed to obtain corresponding holospectra. By using a self-organizing map, the features corresponding to various holospectra were extracted and quantified into metrices as a measure signifying the severity of ball screw misalignment. Experimental results indicated that the proposed method effectively detected the ball screw misalignment even though this misalignment was less than $30\,\mu m$ in size. The experiments conducted in this study demonstrated the high sensitivity and effectiveness of the proposed method, which also has a clear advantage due to its simpler instrumentation compared with traditional accelerometry.

1. Introduction

Shaft misalignment is commonly seen in rotor systems such as feed drive systems, gear sets, and propellers. Shaft misalignment can be divided into two types (Figure 1): angle misalignment, which involves two axes intersecting at an angle, and parallel misalignment, which involves two axes being parallel yet having an offset [1]. In reality, these two types can occur simultaneously. When shaft misalignment occurs in a rotor system, components such as rotors and bearings generate additional vibrations and stresses as they are pulled during their backward and forward movement within the system. After being operated on for a long time, the rotor system experiences fatigue and eventually becomes damaged. For example, when shaft misalignment occurs in the universal joints of a high-speed train, alternating loadings are generated as the system moves back and forth, and these loadings damage the screws [2]. Additionally, shaft misalignment and sliding friction cause vibrations in gear sets and affect gear mesh stiffness, further destabilizing the gear mesh [3]. To prevent shaft misalignment from damaging components and leading to casualties, scholars have generally employed vibration analysis via the rotor dynamics theoretical model and the finite element method (FEM) to study the resulting abnormalities induced by shaft misalignments. For example, Wang ad Gong [4] solved the nonlinear equation derived aiming for a double coupler rotor system using the Newmark-beta method and showed that when parallel misalignment occurred, 2× was obvious in the force spectrum, and 1× and 2× were also obvious in acceleration spectrum. On the other hand, 2× was induced obviously in the displacement spectrum and moment spectrum when the angular misalignment occurred. Nezirić et al. [5] studied different scenarios of misalignments from a rotor system using FEM to reveal that the vibration energy corresponding to multifrequency components and rotor locus increased proportionally to the severity of misalignment.

In 70% of systems with shaft misalignment, the misalignment affects vibration [6, 7]; thus, to diagnose abnormalities in a rotor system, sensors such as accelerometers, displacement sensors, and acoustic emission sensors are typically installed at the ball screw, bearing, gas turbine of the combined cycle power plant, or nut of the
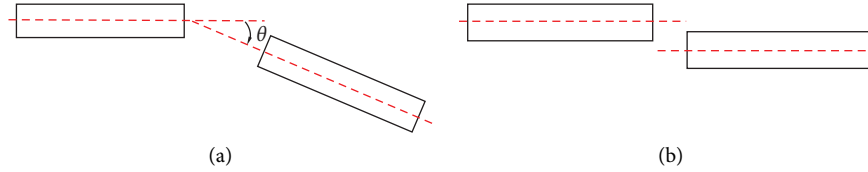
Figure 1: Types of misalignment: (a) angle misalignments and (b) parallel misalignments.

system to obtain vibration signals [7]. The fast Fourier transform (FFT) is often used to obtain the vibration spectrum of the system. The spectrum is then analyzed to see whether it differs from a normal spectrum [8]. Relevant diagnoses can then be made. In the conventional analysis of spectra obtained using FFT, amplitudes and phases corresponding to the speed of the rotor and its multiplier, i.e., 1×, 2×, and 3×, namely, fundamental frequency order (1×), 2nd frequency order (2×), and 3nd frequency order (3×), are most commonly discussed. This is because when shaft misalignment occurs (either parallel or angle misalignment), the amplitudes and phases change substantially [1, 9]. Moreover, when shaft misalignment occurs, the natural frequency of the shaft may be excited, and side bands near the natural frequency are generated. However, when the conventional vibration-based frequency domain method is used to detect abnormalities, the integral transform must be performed, and this transformation is strongly affected by the form and length of the windows in the signals. Additionally, when the rotation speed is not constant, the frequency spectrum is smeared, further lowering the accuracy of measurements of the amplitude and phase of rotor vibration [10]. To overcome this problem, the general approach is to use order tracking, in which the sampling rate is changed according to the change in rotation speed [11]. However, this approach still relies on the FFT using the integral transform and the length of the window still affects the final frequency spectrum analysis result [10].

Other than detecting shaft misalignment by using the conventional FFT frequency spectrum or FFT-based order tracking, researchers have also proposed using the shaft rotating locus to determine the severity of misalignment. The shaft rotating locus can be analyzed using two accelerometers placed perpendicular to each other to measure the vibration of the rotor. Next, order tracking can be employed to extract the amplitudes and phases from the shaft rotational frequency and its frequency multiplier [11]. Then, the amplitudes and phases were used to depict the trajectory of the rotor (similar to an ellipse) at each rotational frequency order, which is called the holospectrum [12]. When the shaft of a feed drive system rotates, coupling occurs and generates lateral vibration called subsynchronous pseudovibration, which reduces the accuracy when assessing shaft misalignment. Thus, when making assessments, in addition to installing displacement sensors in the X and Y directions, a sensor should be installed in the axial direction to increase the accuracy of the holospectrum [13]. Signals of the encoder are used to establish order tracking that is unaffected by rotation speed. Order tracking can increase the accuracy of the holospectrum,

which is higher than when using raw vibration signals for diagnosis [14]. A time-domain order-tracking method called multivariate complex variational mode decomposition (MCVMD) has been proposed. In MCVMD, the Hilbert transform and FFT are used to reconstruct the vibration signals in the X and Y directions to reduce the impact of an unsteady-state complex signal. This method can also be used to decompose the forward and reverse rotation frequency signals. The holospectrum constructed using MCVMD has been verified to be more accurate than that obtained through conventional FFT [15].

In recent years, data-driven diagnostic methods [16], such as traditional machine learning, deep learning, and transfer learning have been employed to diagnose faulty rotodynamic problems. Traditional machine learning such as artificial neural networks (ANN), support vector machine (SVM), and deep neural networks (DNN) have been widely used in mechanical abnormal diagnosis since the 1950s [17, 18]. The vibration, current, acoustic, and temperature signals were collected first [19–22]. Moreover, these methods require features of the time domain or frequency domain. Time-domain features include skewness, standard deviation, mean, and median [23]. Frequency-domain features obtained through FFT or wavelet transform include multiscale entropy and kurtosis [24, 25]. Then, the screening method was used to filter out those features unrelated to machine anomaly. However, the machine health diagnosis relied on engineers' domain knowledge to manually extract the abnormal features. For example, discrete wavelet transform and relief feature screening to normalize vibration signals were employed to increase the accuracy when using an artificial neural network and support vector machine (SVM) to detect misalignment [25]. After using correlation based on feature selection (CFS), adapted correlation based on feature selection (A-CFS), and autoencoder (AE) to screen features, SVM and one-class SVM were also used to detect shaft misalignment [26]. Moreover, feature fusion technology was used to increase the accuracy when using a decision tree classifier, correlation coefficient, and tree regression model to identify shaft misalignment [23]. After a normalized shaft-bearing ellipse orbit has been transformed into two-dimensional images, a multibranch convolutional neural network is suitable for detecting application scenarios of shaft misalignment, which is affected by rotation speed and measurement length [27]. With the advent of deep learning, researchers no longer needed mechanical domain knowledge in machine health diagnosis, which further flourishing intelligent diagnosis techniques [28]. Nevertheless, such an intelligent diagnosis technique based on deep learning requires huge data quantity.

A difficult task in employing machine learning methods is the collection of labelled data, which is either time-consuming or expensive in instrumentation. Therefore, machine health diagnosis using unsupervised algorithms attracted more attention [29–31]. For example, Yan et al. [32] developed an unsupervised online anomaly detection method called hybrid robust convolutional autoencoder (HRCAE), where a fused directional distance (FDD) loss function was calculated with data from multiple sensors to obtain a better ability of detection when the environment had different levels of noise. For an out-of-distribution (OOD) problem that often occurs in practical abnormality diagnosis, Han and Li [33] developed a new detection-assisted fault diagnosis approach for reliable fault diagnosis based on the integration of multiple deep learning networks, i.e., deep ensembles for alerting potentially untrustworthy diagnosis.

The machine health monitoring and diagnosis based on data-driven and deep learning-based methods have achieved convincing results; however, they were often criticized for being accurate for a specific machine or the same type of machine, i.e., lack of generalization. Therefore, researchers have begun to use transfer learning to address this issue. For a more generalized fault feature classifier for rotor fault pattern recognition and diagnosis, the vibration signal feature vector transfer learning was proposed, and the weighted k-nearest neighbor method was presented [34]. For RUL prediction of bearings under multiple operating conditions, the prognostic sensitive features were extracted by a using transfer learning-based bidirectional long short term memory (TBiLSTM) network, and multikernel maximum mean discrepancy (MK-MMD) was proposed [35]. On the other hand, this study proposed that the features are more physically related to the shaft misalignment. That is, the severity of misalignment of the ball screw is quantified according to the features with physical interpretations, i.e., domain knowledge on rotor dynamics.

According to the aforementioned studies, frequency-domain methods involving integral transforms, such as conventional FFT and FFT-based order tracking, are easily limited by the measurement conditions, such as the windowing type of acquired signal and the diagnosis object. Also, although time-frequency domain tacholess order tracking is a method of order tracking in which tachometers are not required, a longer measurement time is typically needed [36]. The research subject of this study was a ball screw feed drive system of which the degree of misalignment is no more than $30\,\mu$m. If we need a higher signal-to-noise ratio of the measured vibration signal, the faster reciprocating speed of the working table is required. However, the travel of the working table was limited (approximately 400 mm); the reciprocal motion of the working table at high-speed thus resulted in vibration signals that were too short. If the ball screw was operated at 1,000 rpm, for the working table to move from 0 to 400 mm took only approximately 1.5 s. When conventional FFT or FFT-based order tracking was applied, the resolution of the frequency spectrum would be low. This was the challenge of this research. Thus, this study adopted VKFOT, which can directly conduct order tracking in the time domain [37]. Without the use of

tachometers, we tracked the amplitude and phase of the ball screw shaft at the rotational frequency and its frequency multiplier.

That is, the severity of misalignment of the ball screw is quantified according to the features with physical interpretations, i.e., domain knowledge on rotor dynamics. The Lissajous curve [13] was utilized to depict the rotor locus at each rotational frequency order. When the ball screw of the feed drive system is misaligned, changes in the rotor locus occur. This study used the features extracted from the rotor trajectory to quantify the severity of the misalignment of a ball screw. In particular, compared with general machine learning methods which mainly rely on statistical features extracted in time or frequency domains, this study proposed the features of ball screw rotational trajectories represented using holospectrum which is more physically related to the shaft misalignment. That is, the severity of misalignment of the ball screw is quantified according to the features with physical interpretations, i.e., domain knowledge on rotor dynamics.

2. Brief Introduction of VKFOT

When the rotor system, such as the bearing, motor mount, or nut, of a feed drive system malfunctions, the amplitude and phase of the rotating shaft at 1× and its frequency multiplier differ from normal, thus, obtaining the vibration features corresponding to the rotation frequency and its frequency multiplier are critical to diagnosing the severity of shaft misalignment. This study employed VKFOT to extract the vibration signal at the rotating shaft frequency and its frequency multiplier in the time domain [37]. The VKFOT approach uses a structure equation and a data equation, both of which assume that noise and the signal for observation are uncorrelated. The least-square method was used to minimize the combined error of the structure equation and data equation, thereby tracking the 1×, 2×, and 3× signals that this study wanted to observe. The structure equation and data equation of VKFOT can be expressed as follows:

$$x_n[k] = q_n[k]b_n[k], \tag{1}$$

$$y[k] = x_n[k] + \eta_n[k], \tag{2}$$

where n is the number of orders; $x_n[k]$ is discretized structural equation consisting of a complex envelope wave of the nth order $q_n[k]$ that we wish to observe; $b_n[k]$ is a carrier wave modulated by the envelope wave $q_n[k]$; and $y[k]$ is the discretized measurement data equation, which is the combination of the discretized structural equation $x_k[k]$ and noise $\eta_k[k]$. Because the carrier wave $b_n[k]$ consists of an order signal, the correlation between the complex carrier wave and each order frequency can be expressed as follows:

$$b_n[k] = e^{\left(2\pi i n \sum_{u=1}^{k} f[u]\Delta T\right)}, \tag{3}$$

where $k = 1, 2, \ldots, N$; N is the total number of data points; $\Delta T = 1/f_s$ is the sampling period; and f_s is the sampling

frequency. The complex envelope wave $q_n(k)$ is expanded by the second-order difference equation as follows:

$$\begin{bmatrix} 1 & -2 & 1 & 0 & \cdots & 0 & 0 & 0 \\ 0 & 1 & -2 & 1 & \cdots & 0 & 0 & 0 \\ \vdots & \vdots & \vdots & \vdots & \ddots & \vdots & \vdots & \vdots \\ 0 & 0 & 0 & 0 & \cdots & 1 & -2 & 1 \end{bmatrix}_{(N-2)\times N} \begin{bmatrix} q_{n(1)} \\ q_{n(2)} \\ \vdots \\ q_{n(N)} \end{bmatrix}_{N\times 1} = \begin{bmatrix} \varepsilon_{n(1)} \\ \varepsilon_{n(2)} \\ \vdots \\ \varepsilon_{n(N)} \end{bmatrix}_{(N-2)\times 1}, \tag{4}$$

where $\varepsilon_n(k)$ is the expanded error item. Equation (4) can be organized into the form of a matrix as follows:

$$\boldsymbol{\Phi}\mathbf{q}_n = \mathbf{E}_n, \tag{5}$$

where $\boldsymbol{\Phi}$ is the coefficient matrix of the second-order difference equation, $\mathbf{q}_n$ is the vector of the envelope wave discrete sequence, and $\mathbf{E}_n$ is the vector of the error discrete sequence. When equation (5) is substituted into equations (1) and (2), the data equation $y[k]$ in the matrix form is as follows:

$$\mathbf{y} = \mathbf{q}_n \mathbf{b}_n + \boldsymbol{\eta}_n, \tag{6}$$

where $\mathbf{q}_n$ is a diagonal matrix, the content of which is the angular displacement of that order, and $\boldsymbol{\eta}_n$ is the error vector of the data equation. The norm of the error vector of the structure equation and the error vector of the data equation are calculated. They are combined using their weights to indicate the total error as follows:

$$\Gamma = r^2 \Gamma_1 + \Gamma_2, \tag{7}$$

where r denotes the weighting factor, which represents the ability of the order-tracking filter to filter out noise, and $\boldsymbol{\Gamma}_1$ and $\boldsymbol{\Gamma}_2$ are the norm values of the data equation and structure equation, respectively:

$$\begin{aligned} \Gamma_1 &= \mathbf{E}_n^{\ H}\mathbf{E}_n = \mathbf{q}_n^{\ H}\boldsymbol{\Phi}^T\boldsymbol{\Phi}\mathbf{q}_n, \\ \Gamma_2 &= \boldsymbol{\eta}_n^{\ H}\boldsymbol{\eta}_n = \left(\mathbf{y}^T - \mathbf{q}_n^{\ H}\mathbf{b}_n^{\ H}\right)\left(\mathbf{y} - \mathbf{b}_n\mathbf{q}_n\right), \end{aligned} \tag{8}$$

where $\mathbf{E}_n$ and $\boldsymbol{\eta}_n$ are the error vectors of the structure equation and the data equation, respectively. To obtain the complex envelope wave $\mathbf{q}_n$ that we want to observe, the total error is minimized during the order-tracking process. The necessary condition is to make the first-order derivative of equation (7) with respect to $\mathbf{q}_n^{\ H}$ equal to 0:

$$\mathbf{q}_n = \left(r^2\boldsymbol{\Phi}^T\boldsymbol{\Phi} + \mathbf{b}_n^{\ H}\mathbf{b}_n\right)^{-1}\mathbf{b}_n^{\ H}\mathbf{y}. \tag{9}$$

This study designed a simulated signal to verify the accuracy of VKFOT with a sampling rate of 1000 Hz and a duration time of 5 s. The relevant parameters are shown in Table 1. This signal consisted of the frequency components corresponding to the rotational frequency and its first four frequency multiplier. Among them, the signal component at 1× was stationary with a fixed amplitude of 10 (the amplitude and phase were both constant); the signal component at 2× was nonstationary with a phase of 20° and amplitude

that linearly increased from 0 to 10 over time; the signal component at 3× was also stationary with a fixed amplitude of 15 but its phase linearly increased from 0° to 90° over time; and the signal component at 4× was a step function with an amplitude of 20 starting from the time at 2.5 sec and with a constant phase of 0°. By using VKFOT, the resulting time-order diagram was obtained (Figure 2) with $r = 1.068 \times 10^7$. The diagram reveals that except for the first 0.1 s after the signal had begun and the 0.1 s before the signal ended, during which all the signal components could be accurately analyzed. At first glance, from the diagram, we may determine that the 1× and 3× signal components had fixed amplitude from 0–5 s; the amplitude of 2× increased over time; and the signal of 4× started at 2.5 s and lasted until the end. However, in the time–order graph of order tracking, the changes in amplitude and phase of 1× and 2× could not be easily observed; thus, a more detailed examination was required. We isolated and extracted the amplitudes and phases of each signal component, as illustrated in Figures 3 and 4.

The amplitude waves from 1× to 3× are the same as shown in the parameters in Table 1. As for 4×, its simulation signal was a step function beginning at 2.5 s. However, VKFOT identified the 4× signal as a quasi-step signal starting at 2.1 s. An additional 0.4 s was required for the amplitude of this signal to increase to 20. The reason was that a combination of a few sine functions could not reconstruct the discontinuity of a signal. Regarding the phase, as illustrated in Figure 4, the 1× and 2× signals had a phase error of approximately 6° compared with the simulated signal. The phase result for 3×, although it had an error compared with the simulated parameters, accurately indicated that its phase increased linearly over time. On the other hand, the phase of 4× exhibited an error of approximately 23.7° compared with the simulated signal. The cause of this large error may have been that the basic function of VKFOT could not easily track signals with discontinuities. In sum, VKFOT was relatively accurate in tracking the amplitude of stationary and non-stationary signals. Regarding phases, because of the filter phase delay and the tracked signal being discontinuous, the results were less accurate. The issue of correcting the phase is explored in the next section.

2.1. Discussion of the Weighting Factor in VKFOT. The weighting factor r in VKFOT not only adjusts the proportion of the structure equation in the overall error Γ, thereby increasing the efficiency of the calculation of convergence,

TABLE 1: Relevant parameter setting for the simulated signal.

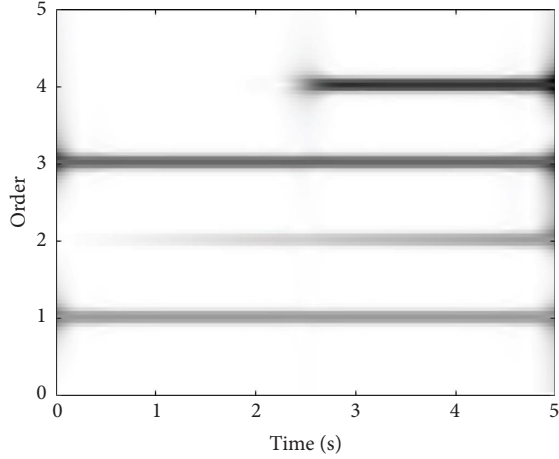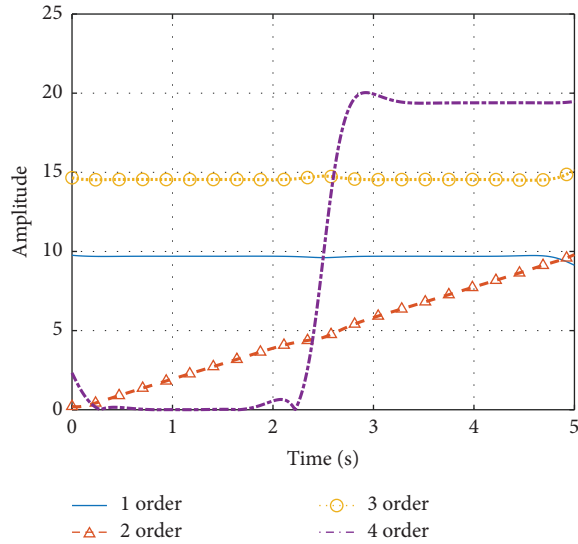| Order (k)	Amplitude (α_k)	Phase (φ_k)
1	10	0°
2	Linear increasing from 0 to 10	20°
3	15	Linear increasing from 0° to 90°
4	$20 \cdot u(t - 2.5) = \begin{Bmatrix} 0, & \text{if } t < 2.5s, \\ 20, & \text{if } t \geq 2.5s, \end{Bmatrix}$	0°

FIGURE 2: Time–step graph of VKFOT (simulated signal).

FIGURE 3: Amplitude of each rotation frequency when using VKFOT (simulated signal).

but also affects the accuracy of VKFOT. Thus, how to determine an optimal r should be addressed first. Because r affects the frequency response of the filter in VKFTO, the polynomial of the frequency response of the energy of the filter can be presented as follows:

$$\left| H\left(e^{j\Omega}\right) \right|^2 = \left| \frac{1}{u_0 + u_1 e^{-j\Omega} + \cdots + u_p e^{-pj\Omega}} \right|^2, \quad (10)$$
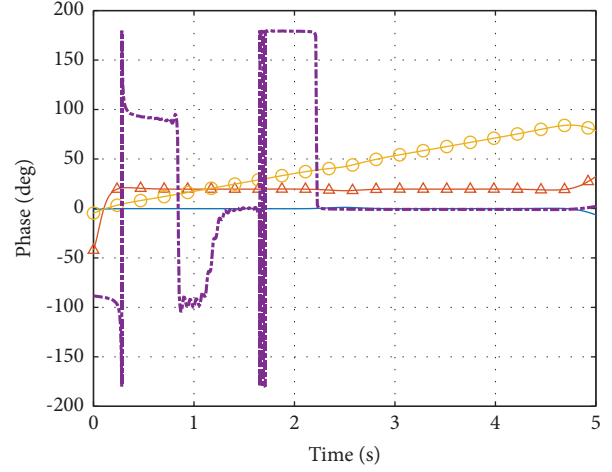

FIGURE 4: Phase of each rotation frequency when using VKFOT (simulated signal).

where $u_0, u_1, \ldots, u_p$ are all variables dependent on r; $\Omega \in (-\pi, \pi)$ is the normalized frequency; and p is the order of the polynomial expansion. Equation (10) shows that adjusting r changes the response of the transfer function. The transfer function corresponding to the effective 3 dB bandwidth is given by the following expression:

$$\left| H\left(e^{j\Omega_b}\right) \right|^2 = \left| \frac{1}{u_0 + u_1 e^{-j\Omega_b} + \cdots + u_p e^{-pj\Omega_b}} \right|^2$$
$$= \frac{1}{\sqrt{2}}, \quad (11)$$

where $\Omega_b = 2\pi(f_b/f_s)$, and f_b is the pass bandwidth. Equation (11) can be reorganized into an equation for r [37] as follows:

$$r = \sqrt{\frac{\sqrt{2} - 1}{\left(2 - 2\cos\left(\Omega_b\right)\right)^2}}. \quad (12)$$

Assuming that the VKFOT is a second-order difference equation, the sampling frequency is 1,000 Hz, and the cutoff frequency f_b is 1 Hz; the transfer function, calculated using equation (10), is then as shown in Figure 5. It is a low-pass filter with narrow bandwidth; in addition to filtering out high-frequency signals, it generates a phase delay (Figure 6). Thus, the phase delay at 1×, 2×, 3×, and 4× of the simulated signal of the transfer function of VKFOT is −174°, −168°,
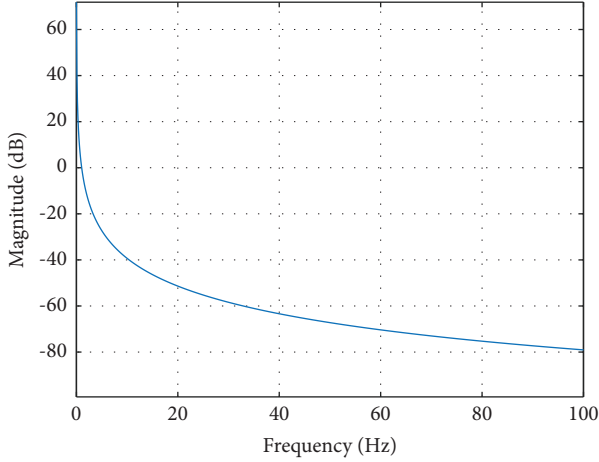
Figure 5: Frequency response in VKFOT (simulated signal).
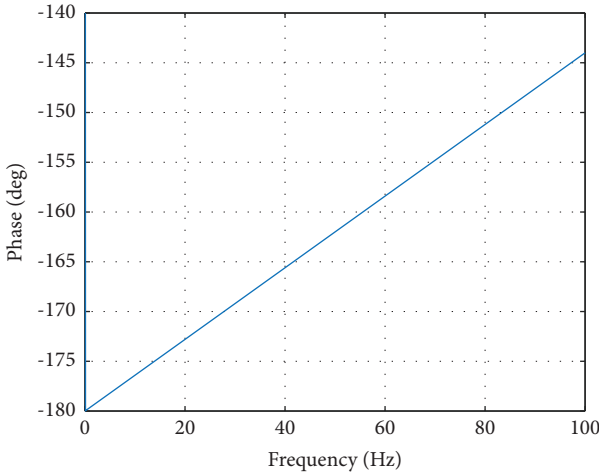

Figure 6: Phase shift in VKFOT (simulated signal).

$-162°$, and $-156°$, respectively. Now, the phase delay of the order signals can be compensated using Figure 6.

It is worth noting that the cutoff frequency f_b of VKFOT should be determined in accordance with the characteristics of the rotor system to be tested. If the selected f_b is too large, the order-tracking process includes a high percentage of noise. If it is too small, the required multiplied frequencies are filtered out by VKFOT. In both situations, the accuracy of VKFOT is low. This study hereby proposed a method for determining whether f_b is determined appropriately. The mean square error (MSE) of the amplitude of the simulated signal and amplitude of VKFOT is defined as follows:

$$\text{MSE}(f_b) = \frac{\|\mathbf{y} - \widehat{\mathbf{y}}\|^2}{N}, \tag{13}$$

where y and $\widehat{\mathbf{y}}$ are the simulated signal and VKFOT tracked signal, respectively, and N is the number of data points. By using equation (13) to minimize the MSE, an appropriate value of fb can be determined.

As mentioned previously, the cutoff frequency f_b of VKFOT should be determined according to the characteristics of the targeted rotor system. Thus, a set of simulation signals were established that were similar to the vibration

signals of an actual ball screw feed system (the targeted rotor system introduced in Section 3). The parameters of the simulated signals are shown in Table 2. The 1× signal was a stationary signal with constant amplitude (0.5 g) and phase (0°). The 2× signal was a nonstationary signal with amplitude increasing linearly from 0 to 0.5 g and a phase of 20°. The 3× signal was a nonstationary signal with amplitude fixed at 0.5 g and a phase increasing linearly from 0° to 90°. The 4× signal was a step function (with an amplitude of 0.5 g) that started at 0.5 s. When f_b was gradually increased from 0.1 to 5 Hz, by using equation (13), we obtained the value of the MSE at different shaft rotational frequency orders. As shown in Figure 7, the four orders of rotational frequency signals had their individual minimum MSE. When the MSE values were averaged (Figure 8), it shows that the smallest mean MSE occurs when $f_b = 1.16$ Hz. After the calculation using equation (12), the corresponding optimal $r = 12115$ in this specific example.

3. Ball Screw Holospectrum Construction and Its Trajectory Feature Extraction

The conventional method of detecting rotor misalignment is to analyze the rotation speed of the frequency domain and changes in amplitude of its multiplied frequencies. However, as stated in [38], this method involves large uncertainties. This study, therefore, explored the detection of the rotor's trajectory in the time domain to quantify the severity of rotor misalignment. The proposed method involves extraction of the holospectrum of each rotation frequency, such as quantifying an elliptical trajectory. As illustrated in Figure 9(a), a dual-axial accelerometer was installed on the nut of a multirotor system to obtain vibration signals in two directions simultaneously. By using VKFOT, the amplitudes and phases of the first three multiplied frequencies were extracted. Coupled with the Lissajous curve, the holospectrum of the motion trajectory of the rotating shaft could be drawn as shown in Figure 9(b) [12]. If the vibration signals along x, y, and z directions were acquired simultaneously by using a triaxial accelerometer, it is worthy of note that the holospectra could be constructed in X–Y plane, Y–Z plane, and X–Z plane, respectively. Each holospectrum represents the motion trajectory of the rotating shaft projected on a specific plane.

This study used these trajectory features to measure and quantify the severity of the misalignment of a ball screw. The Lissajous curve equation can be expressed as follows [13]:

$$x = X \sin(at + \delta), \tag{14}$$

$$y = Y \sin(bt), \tag{15}$$

where x and y are the trajectories in two perpendicular directions; t is the time sequence; X and Y are the amplitude of the vibration signals in the two perpendicular directions; a and b are the frequencies of the vibration signals in the two perpendicular directions; and δ is the phase difference in the vibration signals between the two orthogonal directions.

TABLE 2: Parameter setting for the simulated signal of the verified r value.

Order (k)	Amplitude (α_k)	Phase (φ_k)
1	0.5	0°
2	Linear increasing from 0 to 0.5	20°
3	0.5	Linear increasing from 0° to 90°
4	$0.5 \cdot u(t-2.5) = \begin{cases} 0, & \text{if } t < 2.5s, \\ 0.5, & \text{if } t \geq 2.5s, \end{cases}$	0°
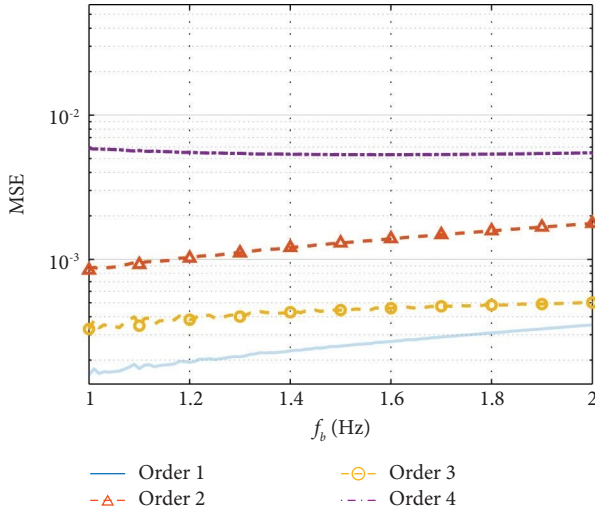
FIGURE 7: Change in the MSE of different orders of the simulated signal under different values of f_b.
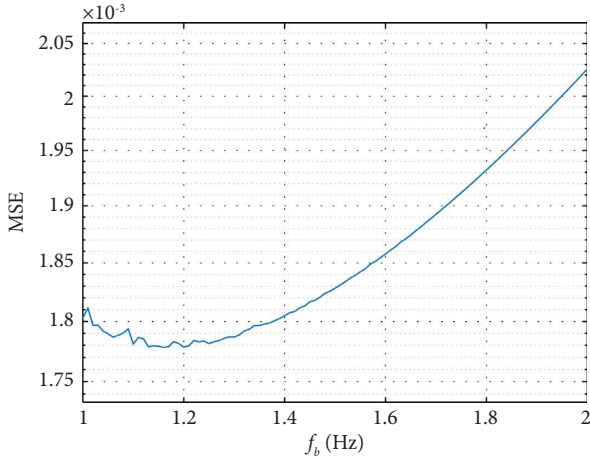
FIGURE 8: Relationship between f_b of the simulated signal and the average MSE.

When $a = b$, equations (14) and (15) can be rewritten as follows:

$$x = X \sin(2\pi ft + \delta), \qquad (16)$$

$$y = Y \sin(2\pi ft), \qquad (17)$$

where f is the shaft rotational frequency established by the holospectrum. The Lissajous elliptic equation of equations (16) and (17) can be converted into a standard elliptic equation represented as follows:

$$\frac{x^2}{X^2} + \frac{y^2}{Y^2} - 2\frac{xy}{XY}\cos\delta = \sin^2\delta. \qquad (18)$$

Equation (18) is organized into the matrix as follows:

$$\begin{bmatrix} x & y & 1 \end{bmatrix} \mathbf{A}_q \begin{bmatrix} x \\ y \\ 1 \end{bmatrix} = 0, \qquad (19)$$

where $\mathbf{A}_q = \begin{bmatrix} A & B & 0 \\ B & C & 0 \\ 0 & 0 & D \end{bmatrix}$, $A = 1/X^2, B = -\cos\delta/XY,$ $C = 1/Y^2$, and $D = -\sin^2\delta$. The relationship between the major and minor axes of the ellipse and eigenvalues of $\mathbf{A}_q$ is as follows:

$$\lambda_1, \lambda_2 = \frac{-\sqrt{2(B^2 - 4AC)D\left((A+C) \pm \sqrt{(A-C)^2 + B^2}\right)}}{B^2 - 4AC}, \qquad (20)$$

where λ_1 and λ_2 are the semimajor and semiminor axes of the ellipse. The relationship of the angle between the major axis of the ellipse and x-axis (i.e., θ, the angle of inclination of the ellipse) with the eigenvector of the ellipse is as follows:

$$\theta = \tan^{-1}\left(\frac{\mathbf{v}_{1y}}{\mathbf{v}_{1x}}\right), \qquad (21)$$

where $\mathbf{V}_{1x}$ and $\mathbf{V}_{1y}$ are the projections of the first eigenvector in the x and y directions, respectively. When λ_1 and λ_2 have been obtained, the eccentricity of the trajectory of the ellipse e can be determined as follows:

$$e = \sqrt{1 - \left(\frac{\lambda_2}{\lambda_1}\right)^2}. \qquad (22)$$

When the ball screw of the feed system is misaligned, changes occur in λ_1, λ_2, θ, e, and the area of the ellipse. This study used these trajectory features to measure and quantify the severity of the misalignment of a ball screw.
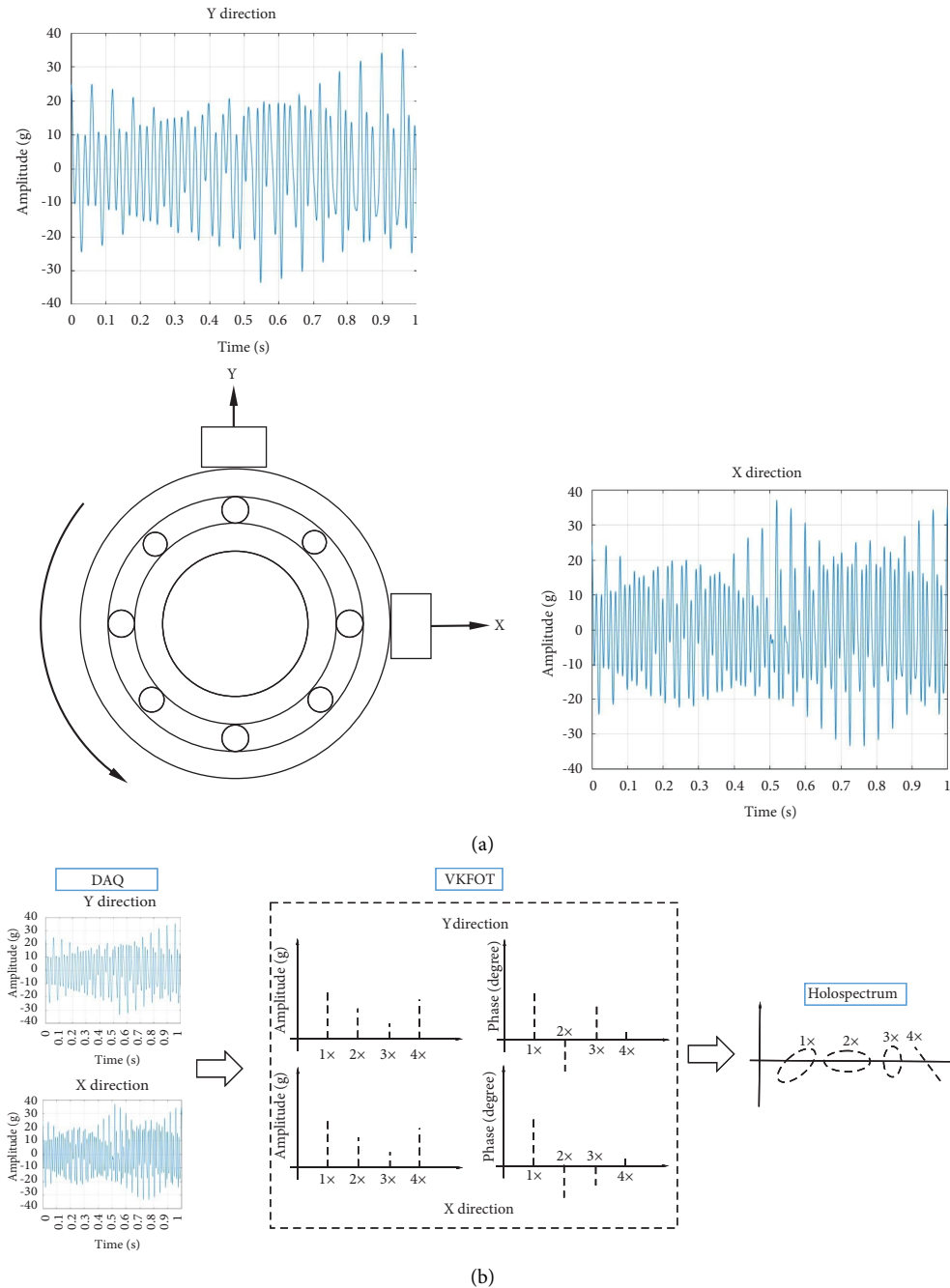
FIGURE 9: Construction of the holospectrum. (a) Vibration signals from accelerometers on bearing. (b) Constructing holospectrum after using VKFOT.

4. Experimental Verification of Ball Screw Misalignment Detection

4.1. Experimental Setup of Ball Screw Misalignment. To verify the effectiveness of the method proposed by this study for detecting misalignment in the ball screw in a feed drive system, this study created a customized ball screw feed drive system (Figure 10). The system comprised a ball screw, a nut, a linear guide way, a working table, front and rear bearings, a motor, and a coupling. The bearing housing located away from the motor end had a device allowing horizontal shifts, which generated misalignment between the bearing housings closer to and further away from the motor and caused the ball screw to bend and shift. The bearing housing located away from the motor was adjusted to have four types of shift—0, 10, 20, and 30 μm—to enable the detection of shaft misalignment of varying severity under the condition of the ball screw shifting no more than 30 μm. The shaft misalignment for the bearing housing adjustment was confirmed using a laser displacement sensor (model: Keyence LK-H025) so that the bearing housing
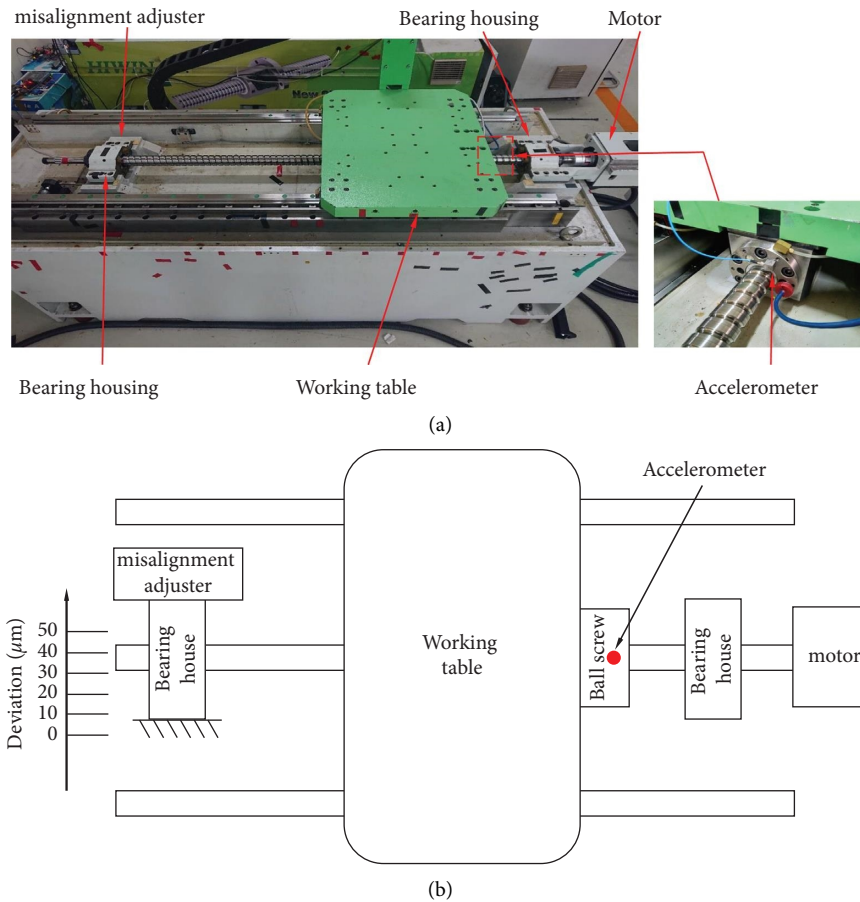
FIGURE 10: Experimental layout of the ball screw shift experiment. (a) Ball screw feed system. (b) Schematic of sensor installation.

was displaced within $\pm 3\,\mu$m when the table moved toward it. To achieve the optimal cost-benefit for diagnosis and to reduce the complexity of the experimental setting, only a triaxial accelerometer (model: PCB 356A02) was installed on the nut. The accelerator both detected ball screw misalignment and diagnosed whether the preload of the nut had disappeared [39].

A rotation speed was set for the working table of this feed drive system. The table automatically moved from 0 to 400 mm back and forth for 15 min. A sampling frequency of 25,600 Hz was adopted to obtain the vibration signal of the three axes at the nut of the feed drive system when it was moving away from the motor at uniform velocity. Notably, when the ball screw was rotated at low speed, a favorable signal-noise ratio could not be obtained. Thus, a high rotation speed was desirable. However, because the travel of the working table was only 0–400 mm, high rotation speed would reduce the measurement length of the vibration signals. Thus, this study found a compromise, with the ball screw made to rotate at 1,000 rpm. Consequently, when the working table moved from 0 to 400 mm, it took approximately 1.5 s. When the durations for acceleration and deceleration were removed, constant-velocity sections of duration 0.78125 s were obtained for measuring signals. Next, by using VKFOT to obtain signals for each order of rotation frequency, the trajectory of ellipses and corresponding holospectra could be established. In addition, features quantifying the trajectories of the

ellipses-such as eccentricity, major and minor axes of the ellipse, the angle of inclination of the ellipse, and the area of the ellipse were calculated.

It is worth noting that changes in temperature cause the deformation of a ball screw. The deformation mainly occurs along the axial direction. However, the thrust effect of the bearing causes the ball screw to bend, which may lead to exacerbated misalignment in the ball screw of the feed drive system. Therefore, this study used the nut temperature as a basis. During each subsequent shift experiment, we used this temperature as the basis for measuring relevant signals, thereby preventing the shift caused by a temperature change from affecting accuracy.

4.2. Detecting Rotor Abnormality Using Self-Organizing Map (SOM).
To compare the diagnosis abilities of VKFOT and conventional FFT-based method regarding the holospectra of shaft misalignment, this study first used 25,600 Hz as the sampling frequency to measure the vibration signal during the work table moving with a constant velocity when the system was under a shift of 0, 10, 20, and 30 μm, respectively. The vibration was measured at the nut when the work table was moving away from the motor, which leads to a signal length of 0.78125 s, defined as a data set hereafter. After incorporating the Hanning window, this study used the FFT

to transform the vibration signal into the frequency domain. After the 60 data sets of vibration frequency spectra of each setting had been averaged, the 1× to 3× signals could be extracted (Figures 11–13, respectively). From Figures 11–13, it shows that the vibration amplitudes corresponding to the first three rotational frequency orders along *x*, *y,* and *z* axes, respectively, distributed randomly for different magnitudes of misalignment, which is difficult to correlate the vibration amplitude and level of severity of rotor misalignments. That is, aiming for detecting ball screw misalignment less than 30 μm with an information collected only using vibration amplitude at different rotational frequency orders based on FFT from a signal length of less than 1 second may lead the diagnosis to inconsistent results. From the signal processing point of view, the VKFOT is proposed to detect the ball screw misalignment for a feed drive system with such a limited travel distance of the work table, i.e., travel distance is less than 1.2 m. The focus of this study lies on signal processing and the associated feature extractions using vibration holospectrum which is more physically related to the shaft misalignment before adopting unsupervised machine learning. The model generalization is believed to be better as compared to those diagnosis methods based on conventional machine learning.

By using VKFOT, the first three rotational frequency orders of vibration signals during the uniform velocity segment lasting 0.78125 s on the nut under the four shift states 0, 10, 20, and 30 μm-in the time domain were obtained. Next, from the holospectra constructed using the signal extracted using VKFOT, features of the resulting trajectory of the ellipse were extracted. A total of 30 data sets at a 0 μm shift were used as the training set, whereas under the shifts of 10, 20, and 30 μm, 10 data sets each were collected as the testing set. Because a holospectrum of multiplied frequency can be projected onto the *X–Y* plane, *Y–Z* plane, and *X–Z* plane and because each plane can yield five features—namely the major and minor axes of the ellipse, eccentricity, the angle of inclination of the ellipse, and area of the ellipse—we could obtain 900,000 features (20,000 (holospectrum) × 3 (plane) × 1 (accelerometer) × 3 (rotational frequency orders) × 5 (features)). A SOM was used for model training [40]. To prevent overfitting, 707 neurons in the SOM were set as a two-dimensional matrix of size 27 × 27 according to the relationship between the data length *L* and neuron number [41]:

$$Z \simeq 5\sqrt{L}, \tag{23}$$

where *Z* is the number of neurons. *K*-fold cross-validation (in this research, *K* = 10) was used for model training, i.e., only for 0 μm data sets in this study. After the diagnosis model had been trained, the minimum quantization error (MQE) was used for quantifying the degree of severity of the shift [42]:

$$\text{MQE} = \|\mathbf{D} - \mathbf{w}_{\text{bmu}}\|, \tag{24}$$

where *D* is the input vector and $\mathbf{w}_{\text{bmu}}$ is the best matching unit (BMU)—closest to the set of 0-μm shift. After *K*-fold cross-validation, equation (24) was applied to the training set to calculate the MQE. As illustrated in Figure 14, the
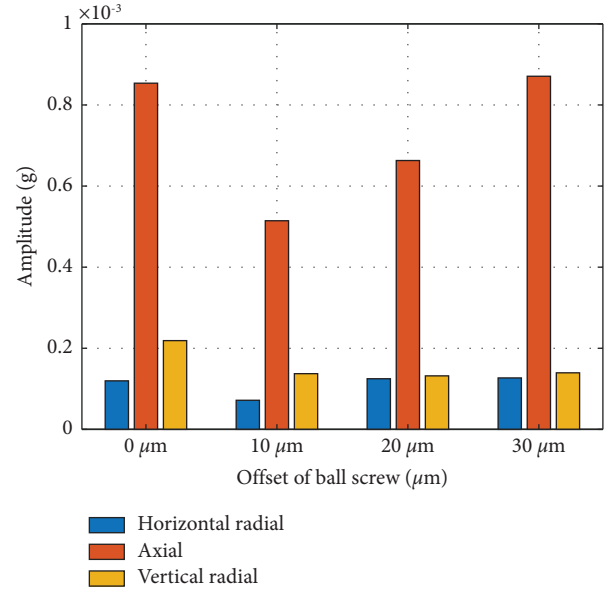

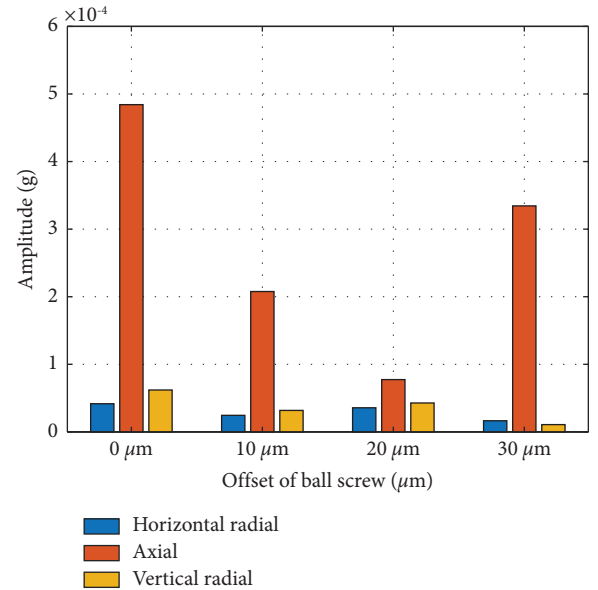FIGURE 11: Amplitude of the nut when the ball screw was under various shifts (1×).

FIGURE 12: Amplitude of the nut when the ball screw was under various shifts (2×).

MQE of the 0 μm shift was steady and approached MQE = 60, which were used as the baseline. The features of the 10 data set each for the 10, 20, and 30 μm shifts were used as the testing set. The MQE of each shift showed a monotonic increase, which exhibits a positive correlation between MQE and the magnitude of the shift. Utilizing the moving average, we could clearly determine that the ball screw using 10 μm as the shift interval (i.e., 0, 10, 20, then 30 μm) had different shift sets. The MQE trend sets of the four groups of shift data were depicted in a box-and-whisker
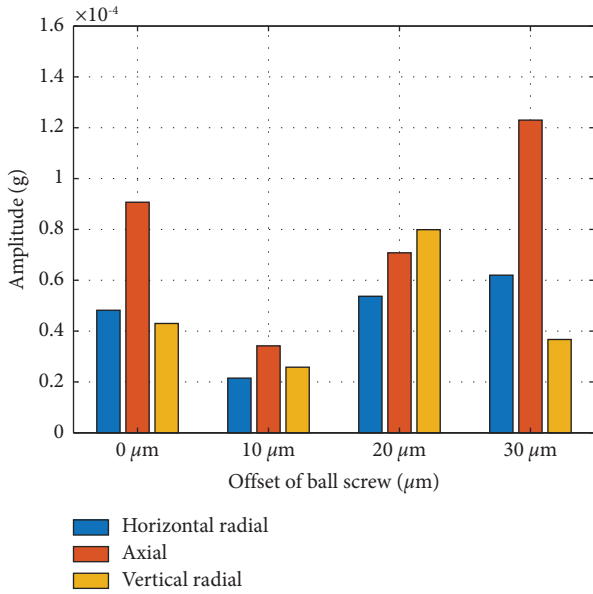
FIGURE 13: Amplitude of the nut when the ball screw was under various shifts (3×).
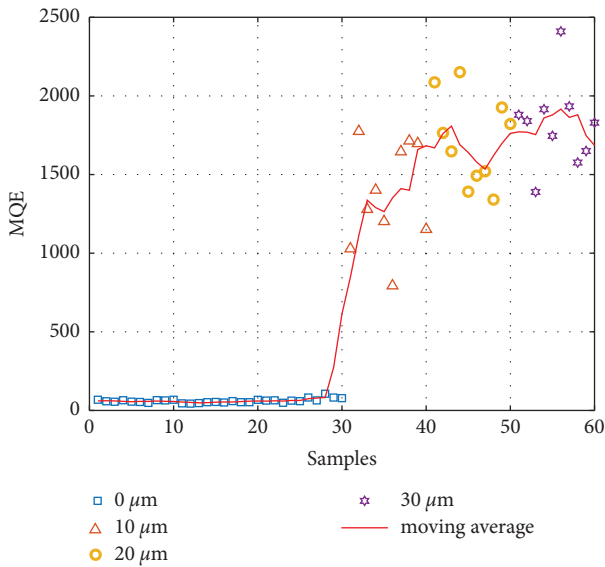

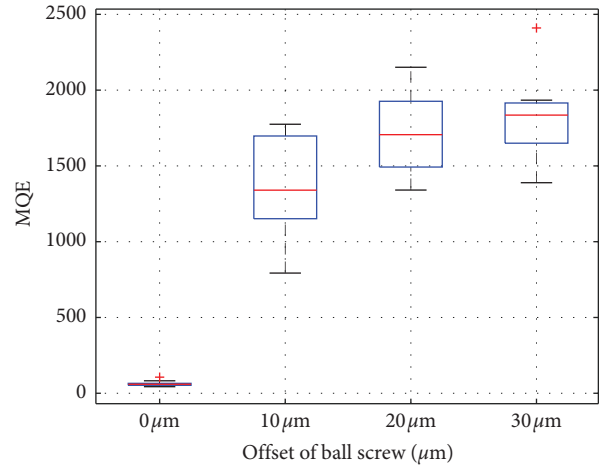FIGURE 14: MQE trend of the ball screw under each shift.

FIGURE 15: MQE box-and-whisker plot of the ball screw under each shift.

The proposed method can be used not only to sense the occurrence of shaft misalignment with high sensitivity but also to quantify the level of misalignment based on similarities and differences between healthy and faulty ball screws, i.e., unsupervised learning. The severity of ball screw misalignment is quantified according to the MQE calculated through SOM. The greater the MQE value is, the more serious shaft misalignment is. As a precautionary measure in monitoring shaft misalignment, thresholds can be defined using the value of MQE according to the severity of shaft misalignment. However, the proposed method after all is an indirect method in detecting the ball screw misalignment as compared to the conventional method to measure the true misalignment directly, such as the dial indicator. Nevertheless, the proposed method has the advantage of easy instrumentation and automated collection of recorded information, which is crucial in the Internet of things (IoT) for daily machine health monitoring.

5. Conclusions

VKFOT was employed to accurately obtain vibration amplitude and phase in the time domain, which provided crucial information for the later construction of vibration holospectra. Simulations using fictitious signals revealed that the vibration amplitude and phase of a time-varying signal could be extracted to sufficiently high accuracy by using VKFOT; however, the associated effectiveness was strongly dependent on the weighting factor r, which was responsible for the phase compensation. Moreover, a fictitious signal that simulated the vibration response of a ball screw nut in a targeted feed drive system was employed to determine the appropriate value of the weighting factor before performing VKFOT for a targeted feed drive system. The features of the corresponding holospectra at the ball screw nut and bearing housings were quantified as metrices to signify in the SOM the level of severity of ball screw misalignment.

Experimental results demonstrated that the proposed method could effectively detect ball screw misalignment when the misalignment caused by the bearing housing was a

plot (Figure 15). This plot revealed that when the shift was $0\,\mu$m, the median MQE was approximately 59.25. When the shift was increased to $10\,\mu$m, the median substantially increased to 1340.02. When the shift was increased to 20 and $30\,\mu$m, the median increased to 1706.16 and 1835.2, respectively. The distance between the first (Q1) and third (Q3) quartiles did not increase as the ball screw misalignment increased. Therefore, when monitoring the severity of ball screw shifts in a feed drive system, the approach of using VKFOT, the features of the ellipse in a holospectrum, the MQE trend in the SOM, the moving average of the MQE shift, and the median of the MQE in the box-and-whisker plot can be employed as a reference to identify misalignment of ball screw under a shift as small as $30\,\mu$m.

shift of 10, 20, or $30 \mu m$, respectively. More specifically, aiming for detecting ball screw misalignment less than $30 \mu m$ with a signal length of less than 1 second, the proposed method proved to be effective in reaching a consistent diagnosis. For such small misalignment, it is worth noting that the experimental validation of the proposed method was conducted when the temperature of the ball screw nut was a specific temperature to prevent the influence of temperature on shaft misalignment.

The experimental validations conducted in this study involved only one type of misalignment; however, the findings demonstrate that the proposed method is more sensitive and effective than traditional spectral analysis in the frequency domain when using traditional accelerometry.

Data Availability

The labelled dataset used to support the findings of this study is available from the corresponding author upon request.

Conflicts of Interest

The authors declare that they have no conflicts of interest.

Acknowledgments

References

[1] M. Desouki, S. Sassi, J. Renno, and S. A. Gowid, "Dynamic response of a rotating assembly under the coupled effects of misalignment and imbalance," *Shock and Vibration*, vol. 2020, Article ID 8819676, 2020.

[2] H. Yongxu, A. C. Tan, C. Liang, and L. Yanping, "Failure analysis of fractured motor bolts in high-speed train due to cardan shaft misalignment," *Engineering Failure Analysis*, vol. 122, Article ID 105246, 2021.

[3] A. Saxena, A. Parey, and M. Chouksey, "Effect of shaft misalignment and friction force on time varying mesh stiffness of spur gear pair," *Engineering Failure Analysis*, vol. 49, pp. 79–91, 2015.

[4] H. Wang and J. Gong, "Dynamic analysis of coupling misalignment and unbalance coupled faults," *Journal of Low Frequency Noise, Vibration and Active Control*, vol. 38, no. 2, pp. 363–376, 2019.

[5] E. Nezirić, S. Isić, I. Karabegović, and A. Voloder, "An analysis of the FEM model of the misaligned rotational system with rotational looseness," *IOSR Journal of Mechanical and Civil Engineering*, vol. 16, no. 2, pp. 29–37, 2019.

[6] T. H. Patel and A. K. Darpe, "Experimental investigations on vibration response of misaligned rotors," *Mechanical Systems and Signal Processing*, vol. 23, no. 7, pp. 2236–2252, 2009.

[7] A. W. K. Fahmi, K. R. Kashyzadeh, and S. Ghorbani, "A comprehensive review on mechanical failures cause vibration in the gas turbine of combined cycle power plants," *Engineering Failure Analysis*, vol. 134, Article ID 106094, 2022.

[8] E. Caso, A. Fernandez-del-Rincon, P. Garcia, M. Iglesias, and F. Viadero, "Monitoring of misalignment in low speed geared shafts with acoustic emission sensors," *Applied Acoustics*, vol. 159, Article ID 107092, 2020.

[9] D. P. Hujare and M. G. Karnik, "Vibration responses of parallel misalignment in Al shaft rotor bearing system with rigid coupling," *Materials Today Proceedings*, vol. 5, no. 11, pp. 23863–23871, 2018.

[10] A. Brandt, T. Lagö, K. Ahlin, and J. Tůma, "Main principles and limitations of current order tracking methods," *Sound and Vibration*, vol. 39, pp. 19–22, 2005.

[11] M. Zhao, J. Lin, X. Wang, Y. Lei, and J. Cao, "A tacho-less order tracking technique for large speed variations," *Mechanical Systems and Signal Processing*, vol. 40, no. 1, pp. 76–90, 2013.

[12] L. Qu, X. Liu, G. Peyronne, and Y. Chen, "The holospectrum: a new method for rotor surveillance and diagnosis," *Mechanical Systems and Signal Processing*, vol. 3, no. 3, pp. 255–267, 1989.

[13] L. Qu, Y. Liao, J. Lin, and M. Zhao, "Investigation on the subsynchronous pseudo-vibration of rotating machinery," *Journal of Sound and Vibration*, vol. 423, pp. 340–354, 2018.

[14] C. Yue and K. Wang, "A fault classification method for rotor under fluctuating condition based on COTHS-CNN," in *Proceedings of the 2020 Asia-Pacific International Symposium on Advanced Reliability and Maintenance Modeling*, no. 1–6, Vancouver, Canada, August 2020.

[15] X. Cui, J. Huang, C. Li, and Y. Zhao, "Three-dimensional instantaneous orbit map for rotor-bearing system based on a novel multivariate complex variational mode decomposition algorithm," *Mechanical Systems and Signal Processing*, vol. 178, Article ID 109211, 2022.

[16] Y. Lei, B. Yang, X. Jiang, F. Jia, N. Li, and A. K. Nandi, "Applications of machine learning to machine fault diagnosis: a review and roadmap," *Mechanical Systems and Signal Processing*, vol. 138, Article ID 106587, 2020.

[17] L. Duan, M. Xie, J. Wang, and T. Bai, "Deep learning enabled intelligent fault diagnosis: overview and applications," *Journal of Intelligent and Fuzzy Systems*, vol. 35, no. 5, pp. 5771–5784, 2018.

[18] R. Liu, B. Yang, E. Zio, and X. Chen, "Artificial intelligence for fault diagnosis of rotating machinery: a review," *Mechanical Systems and Signal Processing*, vol. 108, pp. 33–47, 2018.

[19] J. Ratava, M. Lohtander, and J. Varis, "Tool condition monitoring in interrupted cutting with acceleration sensors," *Robotics and Computer-Integrated Manufacturing*, vol. 47, pp. 70–75, 2017.

[20] G. Li, Y. Fu, D. Chen, L. Shi, and J. Zhou, "Deep anomaly detection for CNC machine cutting tool using spindle current signals," *Sensors*, vol. 20, no. 17, p. 4896, 2020.

[21] C. Zhou, K. Guo, and J. Sun, "Sound singularity analysis for milling tool condition monitoring towards sustainable manufacturing," *Mechanical Systems and Signal Processing*, vol. 157, Article ID 107738, 2021.

[22] T. Li, T. Shi, Z. Tang et al., "Real-time tool wear monitoring using thin-film thermocouple," *Journal of Materials Processing Technology*, vol. 288, Article ID 116901, 2021.

[23] E. C. Yuvaraju, L. R. Rudresh, and M. Saimurugan, "Vibration signals based fault severity estimation of a shaft using machine learning techniques," *Materials Today Proceedings*, vol. 24, pp. 241–250, 2020.

[24] J. L. Lin, J. Y. C. Liu, C. W. Li, L. F. Tsai, and H. Y. Chung, "Motor shaft misalignment detection using multiscale entropy with wavelet denoising," *Expert Systems with Applications*, vol. 37, no. 10, pp. 7200–7204, 2010.

[25] A. M. Umbrajkaar, A. Krishnamoorthy, and R. B. Dhumale, "Vibration analysis of shaft misalignment using machine

learning approach under variable load conditions," *Shock and Vibration*, vol. 2020, Article ID 1650270, 12 pages, 2020.

[26] A. L. Dias, A. C. Turcato, G. S. Sestito, D. Brandao, and R. Nicoletti, "A cloud-based condition monitoring system for fault detection in rotating machines using PROFINET process data," *Computers in Industry*, vol. 126, Article ID 103394, 2021.

[27] X. Yan, C. a. Zhang, and Y. Liu, "Multi-branch convolutional neural network with generalized shaft orbit for fault diagnosis of active magnetic bearing-rotor system," *Measurement*, vol. 171, Article ID 108778, 2021.

[28] E. Golge, "Brief history of machine learning," 2016, https://www.dataversity.net/a-brief-history-of-machine-learning/.

[29] L. M. Elshenawy, M. A. Halawa, T. A. Mahmoud, H. A. Awad, and M. I. Abdo, "Unsupervised machine learning techniques for fault detection and diagnosis in nuclear power plants," *Progress in Nuclear Energy*, vol. 142, Article ID 103990, 2021.

[30] L. C. Brito, G. A. Susto, J. N. Brito, and M. A. V. Duarte, "An explainable artificial intelligence approach for unsupervised fault detection and diagnosis in rotating machinery," *Mechanical Systems and Signal Processing*, vol. 163, Article ID 108105, 2022.

[31] A. Jablonski, M. Bielecka, and A. Bielecki, "Unsupervised detection of rotary machine imbalance based on statistical signal properties," *Mechanical Systems and Signal Processing*, vol. 167, no. 15, Article ID 108497, 2022.

[32] S. Yan, H. Shao, Y. Xiao, B. Liu, and J. Wan, "Hybrid robust convolutional autoencoder for unsupervised anomaly detection of machine tools under noises," *Robotics and Computer-Integrated Manufacturing*, vol. 79, Article ID 102441, 2023.

[33] T. Han and Y. F. Li, "Reliability engineering and system safety," *Out-of-distribution detection-assisted trustworthy machinery fault diagnosis approach with uncertainty-aware deep ensembles*, vol. 226, Article ID 108648, 2022.

[34] S. Wang, Q. Wang, Y. Xiao, W. Liu, and M. Shang, "Research on rotor system fault diagnosis method based on vibration signal feature vector transfer learning," *Engineering Failure Analysis*, vol. 139, Article ID 106424, 2022.

[35] M. S. Rathore and S. P. Harsha, "Rolling bearing prognostic analysis for domain adaptation under different operating conditions," *Engineering Failure Analysis*, vol. 139, Article ID 106414, 2022.

[36] L. Xu, S. Chatterton, P. Pennacchi, and C. Liu, "A tacholess order tracking method based on inverse short time fourier transform and singular value decomposition for bearing fault diagnosis," *Sensors*, vol. 20, no. 23, p. 6924, 2020.

[37] K. S. Wang and P. S. Heyns, "Vold-kalman filter order tracking in vibration monitoring of electrical machines," *Journal of Vibration and Control*, vol. 15, no. 9, pp. 1325–1347, 2009.

[38] A. Shirude and S. Y. Gajjal, "A review on vibration analysis for misalignment of shaft in rotary system by using discrete wavelet transform," *Int. J. Res. Mech. Eng*, vol. 3, pp. 15–19, 2016.

[39] P. C. Tsai, C. C. Cheng, and Y. C. Hwang, "Ball screw preload loss detection using ball pass frequency," *Mechanical Systems and Signal Processing*, vol. 48, no. 1-2, pp. 77–91, 2014.

[40] T. Kohonen, "Essentials of the self-organizing map," *Neural Networks*, vol. 37, pp. 52–65, 2013.

[41] J. Tian, M. H. Azarian, and M. Pecht, "Anomaly detection using self-organizing maps-based k-nearest neighbor algorithm," *PHM Society European Conference*, vol. 2, no. 1, pp. 1–9, 2014.

[42] J. B. Yu and S. Wang, "Using minimum quantization error chart for the monitoring of process states in multivariate manufacturing processes," *Computers & Industrial Engineering*, vol. 57, no. 4, pp. 1300–1312, 2009.